

Eisuke Ueshima, Govindarajan Srimathveeravalli, and
Stephen B. Solomon

Abstract

Irreversible electroporation (IRE) is emerging as an important option for the minimally invasive focal ablation of tumors in the liver, pancreas, prostate, and kidney. Imaging plays a crucial role in selection of appropriate pulse parameters, electrode placement, monitoring of pulse delivery, and evaluating outcomes of IRE. The ability to clearly distinguish between regions of reversible and irreversible electroporation is crucial for the effective treatment of tumors. As electroporation itself cannot be directly visualized in patients, the imaging of tissue changes that arise following electroporation such as changes in perfusion, vascular permeability, diffusion, and functional or metabolic state of tissue is used to monitor IRE in patients. Several imaging techniques, such as computed tomography (CT), ultrasound (US), magnetic resonance imaging (MRI), and positron emission tomography (PET) are now used for guiding and assessing IRE in vivo. In this chapter, typical imaging features that manifest following IRE are discussed and the physiologic effects that underlie these features as seen with different imaging techniques in malignant and normal tissue in the liver, prostate, and other major organs are described.

Keywords

Irreversible Electroporation (IRE) • Computed Tomography (CT) • Magnetic Resonance Imaging (MRI) • Ultrasound (US) • Positron Emission Tomography (PET)

E. Ueshima (✉) • G. Srimathveeravalli • S.B. Solomon
Interventional Radiology Service, Department of Radiology, Memorial Sloan Kettering Cancer Center, New York, NY, USA
e-mail: ueshimae@mskcc.org; srimathS@mskcc.org; SolomonS@mskcc.org

Contents

Introduction	762
Computed Tomography (CT)	763
Ultrasonography (US)	766
Magnetic Resonance Imaging (MRI)	769
Positron Emission Tomography (PET)	773
Conclusions	774
Cross-References	775
References	775

Introduction

Electroporation is a technique used to permeabilize cell membranes with external electric fields. Exposure to an external electric field alters the transmembrane potential of cells and causes formation of nanoscale pores in the bilipid layer. Transient permeabilization of the cell membrane with recovery of membrane integrity with limited or no cell injury is called reversible electroporation (RE) (see ► [Chap. 99, “Electrochemotherapy of Primary Liver Tumors”](#)). RE is an established lab technique, used in the lab and with patients for the introduction of genes and drugs into the cell. Extensive permeabilization of the cell membrane leading to loss of homeostasis and cell death is termed irreversible electroporation (IRE – see ► [Chap. 109, “Safety of Clinical Irreversible Electroporation”](#)). IRE has been developed as an ablation technique for the focal destruction of malignant tumors in solid organs within the clinical setting.

Successful treatment is achieved when the entire tumor and tissue in the tumor margin undergo IRE and not RE. Incomplete IRE of tumors can leave behind residual viable tumor and cause recurrence. In the clinical setting, it is therefore important to discriminate between reversible and irreversible forms of electroporation. Further, IRE requires delivery of high voltage pulses *in vivo*, necessitating careful planning of pulse delivery to targeted tissue and minimizing adverse effects on nontargeted tissue. As permeabilization of cells due to IRE cannot be visualized directly, treatment effects and success is determined by imaging physiological changes associated with successful IRE (see ► [Chap. 109, “Safety of Clinical Irreversible Electroporation”](#)).

Imaging is therefore invaluable to address the needs that come with planning, executing, and evaluating patients following IRE. Medical imaging can be used to simulate treatment before it is even executed, and clinicians can use imaging to plan electrode placement and optimize pulse parameters to ensure adequate tumor coverage. During treatment, imaging can be used to guide the accurate placement of electrodes according to plan and monitor treatment to ensure safety of the patient. Following treatment, imaging can be used to determine treatment efficacy and identify any residual or recurrent tumor. As complications may occur, imaging can also be especially useful for diagnosing any rare complications such as vascular stenoses or thrombus formation that may manifest following IRE.

Several imaging techniques that are used clinically with IRE include ultrasound (US), magnetic resonance imaging (MRI), computed tomography (CT), and positron emission tomography (PET) (Barabasch et al. 2016; Vroomen et al. 2016; Ryan et al. 2013). US and CT are most commonly used with patients to guide electrode placement and monitor pulse delivery. Each imaging modality captures different tissue or physiological changes that manifest from electroporation of tissue. The changes are then interpreted to confirm successful IRE of the targeted tissue. Techniques such as US, CT, MRI, and angiography can accurately capture IRE-related direct tissue effects such as edema, hemorrhage, vascular congestion, tissue necrosis, and devascularization. Techniques such as PET and some MRI sequences can also capture functional tissue changes that arise following IRE such as changes in metabolic changes and tissue perfusion/diffusion in tissue (see ► Chap. 42, “Effect of Electroporation on Blood-Brain Barrier”).

Established techniques for image guided ablation often rely on sustained and large changes in tissue temperature for destruction of tumors and as such they are commonly termed as thermal ablation techniques. On the other hand, while there are transient increases in tissue temperature, cell death from IRE occurs largely from the loss of homeostasis from electroporation of the plasma membrane and not from temperature changes; hence, IRE is termed as a nonthermal ablation technique. Therefore, owing to its nonthermal cell death mechanism, IRE treated tissue can appear different from the findings that manifest following thermal ablation.

Imaging findings following thermal ablation are well documented under multiple modalities; however, current understanding of imaging findings during or following IRE in different organs and tumors is still developing. Thus, in this chapter, the typical features that manifest following IRE, the underlying process captured by different imaging techniques, and the clinical role of these techniques are discussed. Imaging data presented from animal studies were acquired during Institutional Animal Care and Use Committee approved experiments (Table 1).

Computed Tomography (CT)

Computed tomography is one of the most commonly used clinical imaging techniques and utilized for image guided ablation as well. CT makes use of computer-processed combinations of X-ray images acquired from different angles to produce cross-sectional images of the scanned location. These images can be acquired using helical or cone-beam techniques and reconstructed to axial, coronal, and sagittal images.

CT scans can be used for detecting the tumor to be treated with IRE, planning IRE treatment, placing the needle electrodes into the tumor to deliver pulses, and assessing the immediate posttreatment and long-term follow-up outcomes of treatment. On CT scan, air density is defined as -1000 HU (Hounsfield Unit) and water density as 0 HU, with tissue components such as organs, bone, or blood presented in density relative to air and water. Generally, organs and solid tumors are observed to

Table 1 Useful imaging modality of IRE

	Advantage	Shortcoming	Application for treatment planning	Application for treatment monitoring	Application for treatment follow-up
CT	<ul style="list-style-type: none"> • Multi-planar imaging • High resolution 	<ul style="list-style-type: none"> • Radiation 	Essential	Essential for accurate electrode placement	Commonly used
Ultrasound	<ul style="list-style-type: none"> • Portable • Rapid image acquisition • No radiation 	<ul style="list-style-type: none"> • Operator dependent outcomes • Not suitable for imaging deep tissue 	Not useful	Real-time guidance for electrode placement	Useful
MRI	<ul style="list-style-type: none"> • Multi-planar imaging • Functional and metabolic assessment • No radiation 	<ul style="list-style-type: none"> • Imaging susceptible to artifacts • Lengthy acquisition time 	Useful	Not useful	Commonly used
PET (-CT)	<ul style="list-style-type: none"> • Metabolic imaging 	<ul style="list-style-type: none"> • Radiation • Lengthy acquisition time 	Useful	Useful	Useful

be of almost the same density (called soft tissue density) and a contrast agent has to be delivered to assist in differentiating tumor from normal tissue. The contrast agent is typically delivered intravenously; the penetration and washout in normal and tumor tissue vary substantially from differences in vascularization and the patency of the vessels, allowing discrimination of tumor from normal tissue. Hemorrhage in tissue/tumor and bone appear with high density while necrotic tissue and edema appear with low density when compared to normal tissue. Therefore, with CT scans, resultant changes after electroporation such as hemorrhage can be distinguished easily from normal tissue component. Similarly, with contrast enhanced CT, ablation related devascularization of tissue and subsequent necrosis of tissue can be readily imaged. There are several reports describing the imaging features in CT during or after IRE in both normal tissue and tumors. While some imaging findings following IRE appear consistently, other findings do not appear consistently and are yet to be validated as measures for evaluating the effects of IRE.

In the liver tissue ablated with IRE, noncontrast CT shows that ablated lesions are isodense and cannot be clearly delineated immediately following treatment. The same lesions appear hypodense on noncontrast CT at later time points. On dynamic contrast enhanced CT (CECT), IRE lesions immediately after treatment demonstrate 3 zones with different patterns of enhancement: (1) an inner nonenhancing zone, (2) a middle

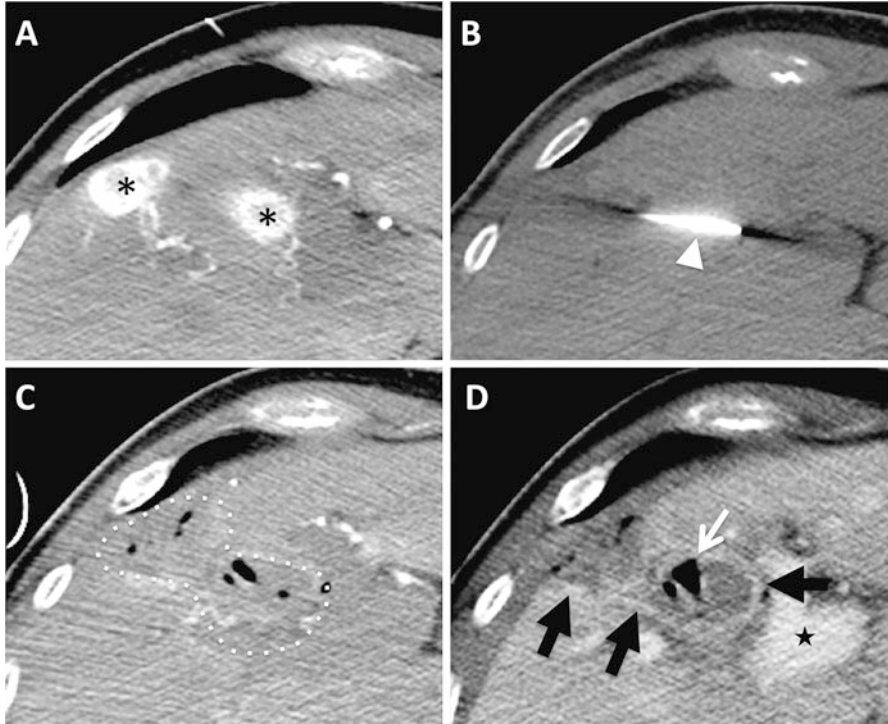


Fig. 1 Contrast enhanced computed tomography (CT) images of liver before and after irreversible electroporation (IRE) of metastatic tumors in a patient. (a) Arterial phase CT image before IRE shows two well-enhanced lesions (*), consistent with metastatic tumors. (b) Noncontrast CT images are used to navigate and place needle electrodes (arrowhead) into one of the lesions. (c) Arterial phase CT image immediately after IRE of two lesions shows heterogeneous united low attenuation of the ablated zones (dotted line) with ill-defined periablational hyperenhancing zones. (d) Portal phase CT image immediately after IRE shows well-demarcated low attenuation of the ablated zones with hyperenhancing zones (black arrows) at the peripheral portion of the ablated lesions. Gas pooling (white arrow) is seen in ablated zone. Portal vein has been annotated with by ★

zone with well-defined progressive internal enhancement, and (3) an outer ill-defined enhancement zone with rapid wash out (Fig. 1c, d). The inner nonenhancing zone exists around the electrode and is understood to demarcate the region of acute necrotic cell death and is similar in appearance to thermal ablation. In the immediate vicinity of the electrodes, cell death from IRE seems to be more immediate and severe than regions that are further away. Also, any thermal effects during IRE are restricted to this region and consequently the tissue may be devascularized, contributing to its appearance on imaging. The middle zone with well-defined progressive internal enhancement is unique to IRE and is not typically observed during imaging of thermal ablation. This region corresponds to tissue where the effects of IRE lead to apoptosis of the tissue with preservation of the vasculature. Preservation of the microvasculature and normal tissue architecture allows penetration of contrast media to this zone, bringing its unique

imaging appearance which is best observed in portal phase CECT. The outermost zone of ill-defined enhancement is consistent with the region of reversible electroporation and vascular hemorrhage just outside the ablation zone (Chung et al. 2016; Lee et al. 2013).

Also in the liver, IRE creates uniform tissue ablation around vasculature and large blood vessels, without perivascular tissue sparing. Although vessel narrowing has sometimes been reported at early imaging follow-up, such imaging features are not observed at later time points. Concurrently, heat sink effects or signs of vascular damage are not observed following IRE (Lee et al. 2012).

IRE of pancreas appears different from IRE of liver. Immediately following treatment, the ablation appears as a uniform hypodense zone and is often substantially larger than the planned ablation. The apparent increase in size of the ablation zone may be related to tissue edema and also because the pancreas is not an encapsulated organ. In contrast to the appearance of IRE ablation in liver, the ablation zone in the pancreas is ill defined, without properly delineated borders. Further, internal enhancement (middle zone) or periablation enhancement (zone of reversible electroporation) are not apparent. Compared to immediate postablation imaging, the treatment region may demonstrate increased enhancement over longer follow-up periods. This may be related to inflammation and the development of granulation tissue and fibrosis (Akinwande et al. 2015).

The key benefits of CT imaging for guiding and follow-up post IRE ablation are its superior spatial resolution, larger field of view, reduced distortion, and rapid image acquisition (Table 2).

Ultrasonography (US)

Ultrasound imaging transmits pulses of high frequency sound waves and produces pictures through patterns of tissue absorption and reflection of the waves. Many different types of images can be formed using US imaging. The most well-known type is a B-mode image, which displays the acoustic properties of a two-dimensional cross section of tissue. In this mode of imaging, features can be strongly echoic (stone, calcification, and gas), hyperechoic (fat, spongy, or necrotic tissue), isoechoic (solid tumor or lesions, surrounded by uniform normal tissue), or echo-free (fluid collections, cysts, and fibrosis). Other forms of US imaging can detect patterns of blood flow (Doppler imaging) or changes in tissue stiffness (elastography). Specifically for IRE, ultrasound is useful for rapid imaging of tumors that are not deeply situated (<10 cm), needle placement with real time imaging, and monitoring of IRE progression. US can also be used for immediate posttreatment assessment of the ablation zone. Several reports have described US imaging features of IRE in the liver.

Thermal ablation of solid tissue, such as liver and kidney, typically causes the treatment zone to appear hyperechoic on B-mode ultrasound. The hyperechoic appearance is typically caused by microbubbles that form in the thermally injured tissue and from tissue desiccation. In contrast, liver ablated IRE presents a hypoechoic zone in the early timing of energy deposition in IRE (Fig. 2a, b). At later acute

Table 2 Imaging features of *computed tomography (CT)* after IRE on liver and pancreas

Liver	CT	Timeline after IRE	Immediately	Later		
		Features	Isodense zone (ill defined)	Hypodense zone (Well defined)		
	Contrast enhanced CT	Timeline after IRE	Immediately ~ few minutes			
		Features	Inner nonenhancing zone	Middle zone with well-defined progressive internal enhancement	Outer ill-defined enhancement zone with rapid wash out	
		Interpretation	Region of acute necrotic cell death	Apoptosis of the tissue with preservation of the vasculature (<i>unique to IRE</i>)	Reversible electroporation and vascular hemorrhage	
	Pancreas	CT	Timeline after IRE	Immediately	Later	
Features			Uniform hypodense zone (ill defined)	Increase in size and less defined		
Contrast enhanced CT		Timeline after IRE	Immediately	Later		
		Features	Hypodense zone (ill defined)	Increased enhancement because of inflammation		

imaging timepoints, this zone decreases in size and becomes more isoechoic (Fig. 2b, c). At 60 min after IRE, the ablation zone appears as a hyperechoic area with a peripheral hyperechoic rim (Fig. 2d). The initial hypoechoic region is caused by water content (i.e., edema) in ablated area as a result of disruption of cellular membrane by IRE. A delayed hyperechoic rim represents widened sinusoidal spaces filled with red blood cells (Lee et al. 2007, 2010; Appelbaum et al. 2014). IRE can sometimes cause microbubbles around electrodes in ablated tissue (Fig. 2a). This may be the result of the formation of hydrogen microbubbles from electrochemical reactions adjacent to the electrodes delivering the electric pulses.

Contrast enhanced ultrasound may provide further benefit for guiding and monitoring treatments by improving depiction of vascularity of the target lesion. On contrast enhanced ultrasound, the IRE ablation zone appears as an enhancing hypovascular area in the arterial phase, in contrast to radiofrequency ablation (RFA) induced thermally coagulated zones which never enhance over time. In the portal phase, a clearly depicted hypovascular area is observed, showing the highest correlation with gross pathologic findings of ablation. In the Kupffer phase (about 10 min after injection of contrast medium), the contrast between IRE ablation zones

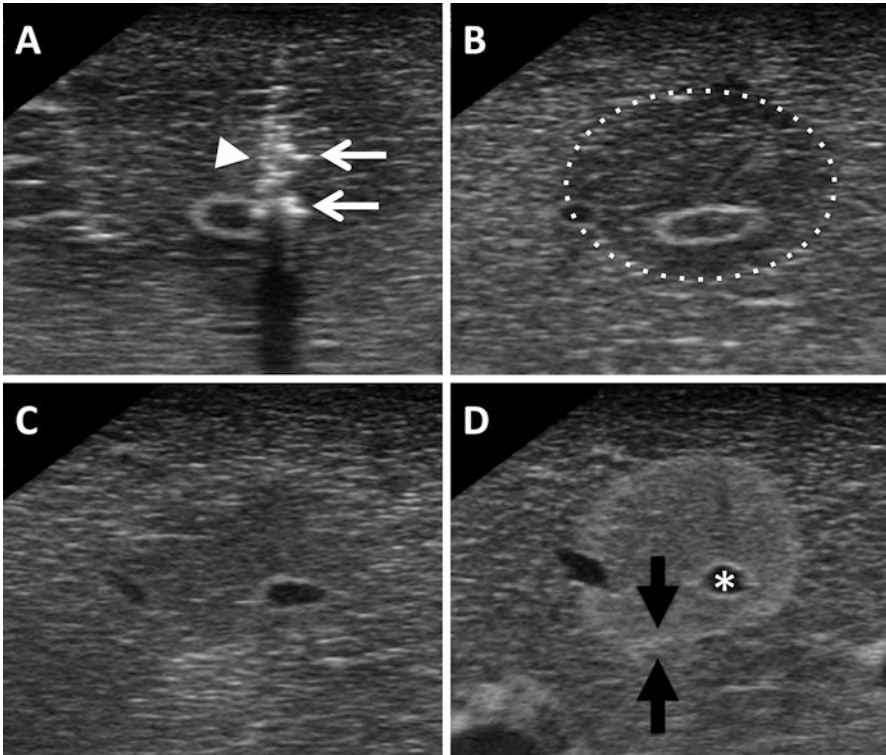


Fig. 2 Typical US findings associated with IRE of normal porcine liver. (a) Scan obtained immediately after IRE with the needle electrode still in place (*arrowhead*). Hyperechoic zone (*white arrows*) seen around the electrode is consistent with “microbubbles.” The needle casts an acoustic shadow (*dark region*) along the needle tract. (b) Scan obtained 1 min after pulse delivery demonstrates a hypoechoic ablative zone (*dotted circle*), with well-demarcated margins. (c) Scan obtained 10 min after ablation demonstrates the hypoechoic ablative zone, decreasing in size. (d) Scan obtained 60 min after procedure shows an ablative zone that has lost the internal hypoechoic zone and with a hyperechoic peripheral rim (*black arrows*). The portal vein is demarcated by an *asterisk*

and liver parenchyma is lower than in portal phase images as a result of faint liver parenchymal enhancement (Sugimoto et al. 2015).

On ultrasound elastography, tissue stiffness can be predicted. Tissue stiffness in the IRE ablation zones increases over time till 4 h posttreatment at which point it plateaus. Tissue stiffness after IRE is less than after radiofrequency ablation and microwave ablation, as the latter are thermal ablation techniques that lead to denaturation of proteins and heat coagulation of ablated tissue while IRE is a nonthermal ablation technique that causes less tissue denaturation (Au et al. 2013).

US imaging presents some unique advantages for guiding and assessing IRE ablations. It can provide images in real-time without risk of ionizing radiation, and the imaging devices are small and portable. However, US may be challenging to

perform in patients with cirrhotic livers as it can be difficult to differentiate tumors from diseased liver (Table 3).

Magnetic Resonance Imaging (MRI)

The movement of protons and the innate magnetic fields found in different elements are used to construct images during MRI. MRI uses magnetic fields and pulses of radio wave energy to excite or perturb protons within the scanner to acquire different types of images. MRI is also capable of performing nonanatomic functional imaging. The movement of protons can be used to determine diffusion, perfusion, or spectroscopic characteristics of living tissue. MRI can employ different imaging sequences such as T1 weighted image, T2 weighted image, fluid attenuation inversion recovery (FLAIR), and diffusion weighted image. Some of these imaging sequences can be combined with the use of intravenously administered MR imaging contrast to enhance image acquisition. Therefore, MRI can provide superior anatomic detail as well as contrast and functional status of IRE treated tissue.

Electroporation, IRE-related permeabilization of cell membrane, as well as secondary effects on microvasculature can cause fluid changes in the treated location. These changes in turn cause edema, hemorrhage, or congestion, all of which can be readily visualized with different MRI sequences. Generally, on T1 weighted image, tissue hemorrhage appears as a region of high signal intensity. At the same time, edema, congestion, and residual tumor all demonstrate high signal intensity on T2 weighted and FLAIR sequences. On diffusion weighted images, viable tumor and infarction of tissue restrict the movement of protons and can be seen as regions with high signal intensity. However, these typical intensities of MRI are not always seen after electroporation and depend on the tissue (including its water and vascular flow) and timing of image acquisition after electroporation.

MRI features after electroporation can vary substantially based on the tissue or organ being treated and change considerably over time following electroporation. At acute phase, images on MRI are usually influenced by the presence of edema and hemorrhage. At later time points, presence of inflammation, fibrosis, and tissue remodeling determines imaging findings.

In potato (vegetable) ablated with IRE, the ablated lesion can be seen as a high intensity area. The lipids in potato tissue are in the intact cell membrane and are organized in a tight structure, and protons in the molecule cannot vibrate freely. When molecular defects are induced in the cell membrane, the lipids in the membrane have additional degrees of freedom, resulting in a higher signal in T1 weighted image and FLAIR sequence images, which suppress the effects of the liquid and enhance the effects of lipids (Hjouj and Rubinsky 2010).

In liver ablated with IRE, ablation zones are immediately visible on MR images as hypointense regions on T1 weighted images, and appear as homogeneously hyperintense regions when compared with normal liver parenchyma on T2 weighted images and as hyper/iso-intense (relative to adjacent normal liver parenchyma) regions on proton density weighted images (Zhang et al. 2010; Guo et al. 2010). Signal intensity

Table 3 Imaging features of *ultrasound* after IRE on liver

Ultrasound	Timeline after IRE	Immediately	~ Few minutes	~10 min	Around 60 min
	Features	Microbubbles around electrode	Hypoechoic zone	Decreases in size and becomes more isoechoic	Hyperechoic area with a peripheral hyperechoic rim
	Interpretation	Hydrogen microbubbles from electrochemical reactions	Treatment related changes in tissue water content	Widened sinusoidal spaces being filled with red blood cells	
Contrast enhanced ultrasound	Timeline after IRE	Immediately ~ few minutes Arterial phase	Portal phase	Kupffer phase (about 10 min after contrast injection)	
	Features	Enhancing hypovascular area	Clearly depicted hypovascular area	Contrast between IRE ablation zones and liver parenchyma is lower	
	Interpretation	Preserved vasculature, not observed in thermal ablation	Clear demarcation of necrotic regions	Result of faint liver parenchymal enhancement	

of the ablation zone on T2 weighted image becomes intermediately hypointense compared with normal parenchyma and exhibits a hyperintense rim that is visible around the ablation zone. Contrast-enhanced MRI visualizes the ablated lesion as a hyperintensity area on T1 weighted images. This hyperintensity area, however, includes both reversible and irreversible regions, resulting in overestimating of ablated region. Penumbra-nulled IR images (inversion times set to null signal from peripheral penumbra surrounding ablation zone) seem to provide more accurate predictions of IRE ablation zones than contrast enhanced T1 weighted image (Guo et al. 2011).

In hepatocellular carcinoma lesions ablated with IRE, a hyperintense core and a hypointense rim are observed on T1 weighted images. On T2 weighted images, the signal is heterogeneously hypointense. On diffusion weighted imaging (DWI), the signal is not clearly discernible even for different b values (Granata et al. 2015). Signal intensity of liver lesions immediately following IRE appears similar to signal intensity on pretreatment imaging (Barabasch et al. 2016).

In prostate tissue 2–4 weeks after IRE, the ablated zone appears as a heterogeneous hypointense zone on the follow-up T1 weighted images (Fig. 3b), but it is not clear enough to separate the ablated region from surrounding normal tissue. On T2 weighted images, the ablation zone appears as a hyperintense area interspersed with low intensity area (Fig. 3c). On contrast-enhanced T1 weighted images, the ablated area clearly appears as nonenhancing (Srimathveeravalli et al. 2016) (Fig. 3d). Although both T2 weighted images and contrast-enhanced T1 weighted images are useful to identify the ablation zone, T2 weighted images are influenced by edema and inflammation. Therefore, contrast enhanced T1 weighted images seem to provide a more accurate prediction of IRE ablation zone than T2 weighted images (van den Bos et al. 2016).

Pancreas and pancreatic tumor treated with IRE can be seen as an ill-defined region, as heterogenous hyperintense appearance on T2 weighted images, and as an isointense region on T1 weighted images. These image findings can be associated with limited healthy parenchyma surrounding the tumor and from treatment related edema. The treated regions are not clearly discernible on diffusion weight images and on contrast enhanced T1 weighted imaging (Vroomen et al. 2016).

In kidney ablated with IRE, the highest visual contrast between the treatment zone and normal parenchyma can be obtained by fat-suppressed T2 weighted image. Treatment region show inhomogeneous necrosis with small perifocal edema in the short-term and sharply demarcated scars in the mid-term. The central necrotic regions appear isointense when compared to the adjacent renal cortex on T2 weighted image and diffusion weighted image and hypointense on T1 weighted image (Wendler et al. 2013).

In the brain of rats, diffusion weighted imaging is capable of detecting electroporation-induced permeabilization of brain tissue. In the diffusion weighted images, permeabilized area of brain tissue shows hyperintensity after electroporation (Mahmood et al. 2015). On the other hand, in the brain of dogs, blood brain barrier disruption appears as a zone of clear enhancement on T1 weighted images. Diffusion weighted images shows no significant changes in blood brain barrier. Early treatment effects and late irreversible damage are clearly depicted as hyperintensity on the T2 weighted images (Hjouj et al. 2012). IRE ablation zones are sharply demarcated and iso- to hypointense on the T1 weighted image sequences, hyperintense on T2

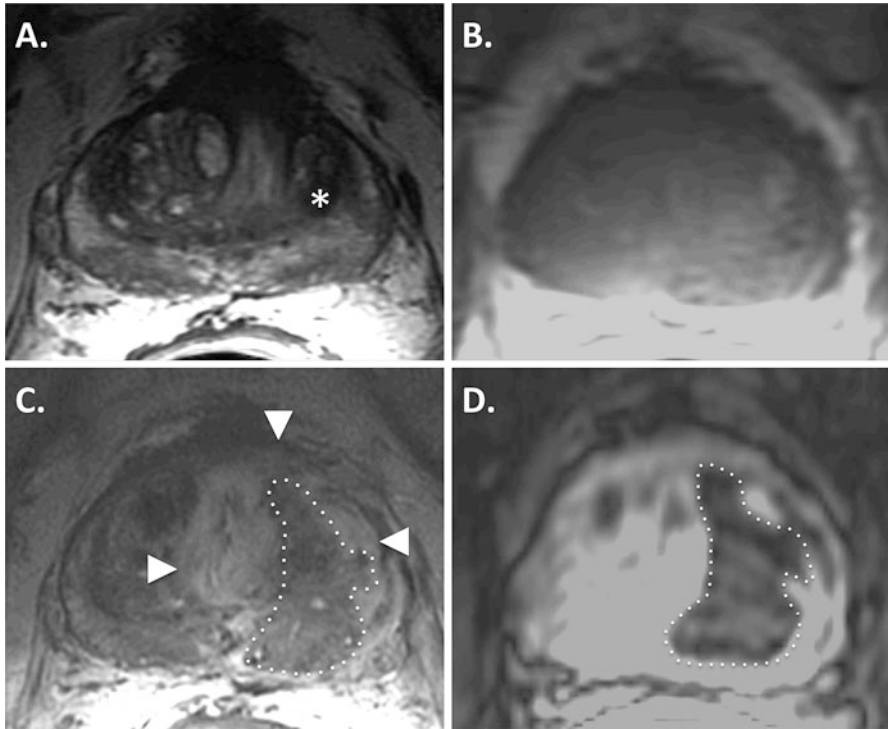


Fig. 3 Representative MR images of patient prostate treated with IRE (a) and 2 weeks after (b, d) IRE. (a) T2 weighted image before treatment shows hypointense tumor (*) in the left lobe of prostate. (b) Ablated zone appears isointense and cannot be clearly separated from surrounded normal prostate on T1 weighted images. (c) Ablated zone appears as a heterogeneous hyperintense region (arrowheads) with an internal hypointense region (*dotted area*) on T2 weighted images. Hypointense region shows an irreversible ablated area, whereas hyperintense region shows possibly reversible area, associated with inflammation and edema. (d) Contrast enhanced T1 weighted images show nonenhancing region (*dotted area*). This region demonstrates a completely ablated area, matching the hypointense region on T2 weighted images ((c))

weighted images, and peripherally contrast enhancing following intravenous administration of Gadolinium contrast media (Ellis et al. 2011).

While CT, MRI, and US are used for assist in the setting of electroporation, they are unable to monitor the process of pulse delivery or localize the electric field for more accurate focal treatments. Magnetic resonance with electric impedance tomography may reconstruct electric field distribution to images by measuring the electric current density distribution and electric conductivity of the treated subject during application of electric pulses. MR electric impedance tomography can thus be used for the prediction of reversibly and irreversibly electroporated areas (Kranjc et al. 2015) (Table 4).

Table 4 Imaging features of *magnetic resonance imaging (MRI)* after IRE

Liver	Timeline after IRE	Immediately		
	Sequences	T1 weighted image	Contrast enhanced T1 weighted image	T2 weighted image
	Features	Hypointense zone	Hyperintense zone	Hyperintense zone
	Interpretation	-	Includes both reversible and irreversible areas	-
Prostate	Timeline after IRE	2–4 weeks		
	Sequences	T1 weighted image	Contrast enhanced T1 weighted image	T2 weighted image
	Features	Hypointense zone (ill defined)	Nonenhancing zone	Hyperintense zone with an internal hypointense zone
	Interpretation	-	Irreversible zone	Internal hypointense zone matches with irreversible zone

Positron Emission Tomography (PET)

Positron emission tomography (PET) uses small amounts of radioactive materials called radiotracers. These radiotracers are taken up in relevant organs or tumors, and a special radiation detector evaluates organ and tissue functions, such as blood flow, oxygen use, and glucose metabolism. The most popular tracer is 2-deoxy-2-[fluorine-18]fluoro- D-glucose (^{18}F -FDG). ^{18}F -FDG PET provides functional imaging based on the increased glucose uptake of tissue and depicts metabolic abnormalities before morphological alterations occur. Because cancer grows at a faster rate than healthy tissue and inflammation needs more glucose, cancer cells and inflammation absorb more ^{18}F -FDG. PET scanner detects the radiation given off by the ^{18}F -FDG and produces color-coded images showing inflammation and cancer tissue. Currently, many PET scanners also include a conventional computed tomography (CT) scanner. This allows images of both anatomy (CT) and function (PET) to be taken during the same examination.

Tissue that has been destroyed with thermal ablation become metabolically inactive and does not take up ^{18}F -FDG. Recurrence and residual lesions then show up as regions of intense ^{18}F -FDG uptake.

PET scans of IRE ablation demonstrate a dynamic response to the IRE ablation. At a few hours following IRE, completely ablated area has no uptake of ^{18}F -FDG. However, at a few days following IRE therapy, uptake of ^{18}F -FDG surrounding the ablated region can be seen. At one month or after following IRE, this peripheral

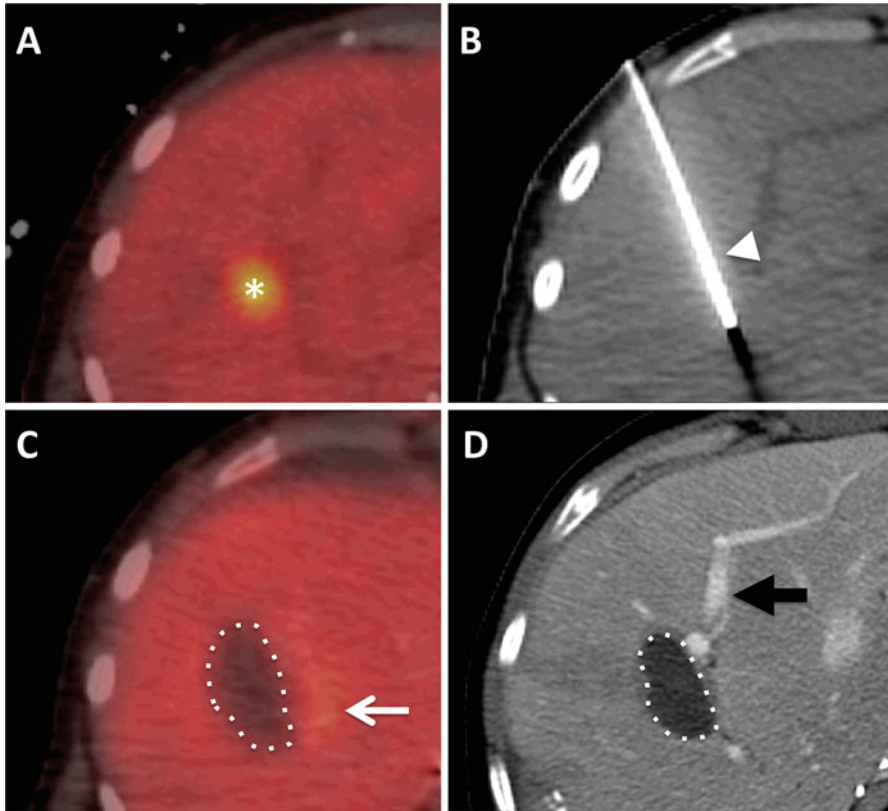


Fig. 4 Positron emission tomography (PET) CT of IRE ablation of metastatic liver tumor in a patient. (a) Preablation image shows ^{18}F -FDG uptake (*) in the right lobe of liver, demonstrating a metastatic lesion from colorectal cancer. (b) The FDG avid lesion is used as an aid to guide electrode (*arrowhead*) placement into the tumor. (c) At one month post-IRE, the treated region demonstrates faint ^{18}F -FDG uptake (*white arrow*) lower than surrounding liver indicating metabolically inactive tissue in the ablated region (*dotted area*). (d) At three month post-IRE, contrast enhanced CT shows a hypodense zone (*dotted area*) and no recurrence. Portal vein is identified with a *black arrow*

increase in FDG uptake is no longer present (Fig. 4). Increase of uptake at a few days around the IRE region may be due to an inflammatory response increasing metabolic activity. Therefore, an accurate assessment of IRE treatment with PET should be performed after inflammation has resolved (Ryan et al. 2013; Neal et al. 2012).

Conclusions

In this chapter, typical imaging features that can be observed with different imaging techniques following electroporation of normal and malignant tissue has been described. Image guidance is crucial for planning and monitoring IRE treatment as

well as reviewing the efficacy of treatment and evaluating for recurrences after IRE. Imaging features after electroporation can vary substantially based on the tissue or organ being treated and changes considerably over time following electroporation. While some of the imaging features are similar to what is observed following thermal ablations, IRE demonstrates other unique features that are specific to this ablation technique. As a relatively new clinical technique, our understanding of tissue effects of IRE seen on imaging is still growing and our ability to accurately monitor treatment with IRE will improve in the future.

Cross-References

- ▶ [Effect of Electroporation on Blood-Brain Barrier](#)
- ▶ [Electrochemotherapy of Primary Liver Tumors](#)
- ▶ [Safety of Clinical Irreversible Electroporation](#)

References

- Akinwande O, Ahmad SS, Van Meter T, Schulz B, Martin RC (2015) CT findings of patients treated with irreversible electroporation for locally advanced pancreatic cancer. *J Oncol* 2015:680319. doi:10.1155/2015/680319
- Appelbaum L, Ben-David E, Faroja M, Nissenbaum Y, Sosna J, Goldberg SN (2014) Irreversible electroporation ablation: creation of large-volume ablation zones in in vivo porcine liver with four-electrode arrays. *Radiology* 270(2):416–424. doi:10.1148/radiol.13130349
- Au JT, Kingham TP, Jun K, Haddad D, Gholami S, Mojica K, Monette S, Ezell P, Fong Y (2013) Irreversible electroporation ablation of the liver can be detected with ultrasound B-mode and elastography. *Surgery* 153(6):787–793. doi:10.1016/j.surg.2012.11.022
- Barabasch A, Distelmaier M, Heil P, Krämer NA, Kuhl CK, Bruners P (2017) Magnetic resonance imaging findings after percutaneous irreversible electroporation of liver metastases: a systematic longitudinal study. *Investig Radiol* 52(1):23–29
- Chung DJ, Sung K, Osuagwu FC, Wu HH, Lassman C, Lu DS (2016) Contrast enhancement patterns after irreversible electroporation: experimental study of CT perfusion correlated to histopathology in normal porcine liver. *J Vasc Interv Radiol* 27(1):104–111. doi:10.1016/j.jvir.2015.09.005
- Ellis TL, Garcia PA, Rossmeisl JH Jr, Henao-Guerrero N, Robertson J, Davalos RV (2011) Nonthermal irreversible electroporation for intracranial surgical applications Laboratory investigation. *J Neurosurg* 114(3):681–688. doi:10.3171/2010.5.JNS091448
- Granata V, Fusco R, Catalano O, Piccirillo M, De Bellis M, Izzo F, Petrillo A (2015) Percutaneous ablation therapy of hepatocellular carcinoma with irreversible electroporation: MRI findings. *AJR Am J Roentgenol* 204(5):1000–1007. doi:10.2214/AJR.14.12509
- Guo Y, Zhang Y, Klein R, Nijm GM, Sahakian AV, Omary RA, Yang GY, Larson AC (2010) Irreversible electroporation therapy in the liver: longitudinal efficacy studies in a rat model of hepatocellular carcinoma. *Cancer Res* 70(4):1555–1563. doi:10.1158/0008-5472.CAN-09-3067
- Guo Y, Zhang Y, Nijm GM, Sahakian AV, Yang GY, Omary RA, Larson AC (2011) Irreversible electroporation in the liver: contrast-enhanced inversion-recovery MR imaging approaches to differentiate reversibly electroporated penumbra from irreversibly electroporated ablation zones. *Radiology* 258(2):461–468. doi:10.1148/radiol.10100645
- Hjouj M, Rubinsky B (2010) Magnetic resonance imaging characteristics of nonthermal irreversible electroporation in vegetable tissue. *J Membr Biol* 236(1):137–146. doi:10.1007/s00232-010-9281-2

- Hjouj M, Last D, Guez D, Daniels D, Sharabi S, Lavee J, Rubinsky B, Mardor Y (2012) MRI study on reversible and irreversible electroporation induced blood brain barrier disruption. *PLoS One* 7(8):e42817. doi:10.1371/journal.pone.0042817
- Kranjc M, Markelc B, Bajd F, Čemažar M, Serša I, Blagus T, Miklavčič D (2015) In situ monitoring of electric field distribution in mouse tumor during electroporation. *Radiology* 274(1):115–123. doi:10.1148/radiol.14140311
- Lee EW, Loh CT, Kee ST (2007) Imaging guided percutaneous irreversible electroporation: ultrasound and immunohistological correlation. *Technol Cancer Res Treat* 6(4):287–294
- Lee EW, Chen C, Prieto VE, Dry SM, Loh CT, Kee ST (2010) Advanced hepatic ablation technique for creating complete cell death: irreversible electroporation. *Radiology* 255(2):426–433. doi:10.1148/radiol.10090337
- Lee YJ, Lu DS, Osuagwu F, Lassman C (2012) Irreversible electroporation in porcine liver: short- and long-term effect on the hepatic veins and adjacent tissue by CT with pathological correlation. *Investig Radiol* 47(11):671–675. doi:10.1097/RLI.0b013e318274b0df
- Lee YJ, Lu DS, Osuagwu F, Lassman C (2013) Irreversible electroporation in porcine liver: acute computed tomography appearance of ablation zone with histopathologic correlation. *J Comput Assist Tomogr* 37(2):154–158. doi:10.1097/RCT.0b013e31827dbf9b
- Mahmood F, Hansen RH, Agerholm-Larsen B, Gissel H, Ibsen P, Gehl J (2015) Detection of electroporation-induced membrane permeabilization states in the brain using diffusion-weighted MRI. *Acta Oncol* 54(3):289–297. doi:10.3109/0284186X.2014.991045
- Neal RE II, Cheung W, Kavounoudias H, Thomson KR (2012) Spectrum of imaging and characteristics for liver tumors treated with irreversible electroporation. *Biomed Sci Eng* 5:813–818. doi:10.4236/jbise.2012.512A102
- Ryan ER, Sofocleous CT, Schöder H, Carrasquillo JA, Nehmeh S, Larson SM, Thornton R, Siegelbaum RH, Erinjeri JP, Solomon SB (2013) Split-dose technique for FDG PET/CT-guided percutaneous ablation: a method to facilitate lesion targeting and to provide immediate assessment of treatment effectiveness. *Radiology* 268(1):288–295. doi:10.1148/radiol.13121462
- Srimathveeravalli G, Cornelis F, Mashni J, Takaki H, Durack JC, Solomon SB, Coleman JA (2016) Comparison of ablation defect on MR imaging with computer simulation estimated treatment zone following irreversible electroporation of patient prostate. *Springerplus* 5:219. doi:10.1186/s40064-016-1879-0
- Sugimoto K, Moriyasu F, Kobayashi Y, Kasuya K, Nagakawa Y, Tsuchida A, Hara T, Iobe H, Oshiro H (2015 Feb) Assessment of various types of US findings after irreversible electroporation in porcine liver: comparison with radiofrequency ablation. *J Vasc Interv Radiol* 26(2): 279.e3–287.e3. doi:10.1016/j.jvir.2014.11.007
- van den Bos W, de Bruin DM, van Randen A, Engelbrecht MR, Postema AW, Muller BG, Varkarakis IM, Skolarikos A, Savci-Heijink CD, Jurhill RR, Zondervan PJ, Laguna Pes MP, Wijkstra H, de Reijke TM, de la Rosette JJ (2016 Jul) MRI and contrast-enhanced ultrasound imaging for evaluation of focal irreversible electroporation treatment: results from a phase I-II study in patients undergoing IRE followed by radical prostatectomy. *Eur Radiol* 26(7): 2252–2260. doi:10.1007/s00330-015-4042-3
- Vroomen LG, Scheffer HJ, Melenhorst MC, de Jong MC, van den Bergh JE, van Kuijk C, van Delft F, Kazemier G, Meijerink MR (2016) MR and CT imaging characteristics and ablation zone volumetry of locally advanced pancreatic cancer treated with irreversible electroporation. *Eur Radiol*. Epub ahead of print. PMID:27659702. doi:10.1007/s00330-016-4581-2
- Wendler JJ, Porsch M, Hühne S, Baumunk D, Buhtz P, Fischbach F, Pech M, Mahnkopf D, Kropf S, Roessner A, Ricke J, Schostak M, Liehr UB (2013) Short- and mid-term effects of irreversible electroporation on normal renal tissue: an animal model. *Cardiovasc Intervent Radiol* 36(2): 512–520. doi:10.1007/s00270-012-0452-7
- Zhang Y, Guo Y, Ragin AB, Lewandowski RJ, Yang GY, Nijm GM, Sahakian AV, Omary RA, Larson AC (2010) MR imaging to assess immediate response to irreversible electroporation for targeted ablation of liver tissues: preclinical feasibility studies in a rodent model. *Radiology* 256(2):424–432. doi:10.1148/radiol.10091955